RSC Advances

PAPER

View Article Online
View Journal | View Issue

Check for updates

Cite this: *RSC Adv.*, 2017, **7**, 41228

Efficient removal of Pb(II) ions using manganese oxides: the role of crystal structure

Haipeng Zhang, Anbang Wu, Heyun Fu, Ling Zhang, Hui Liu, Shourong Zheng, Haiqin Wan and Zhaoyi Xu *

Received 27th May 2017
Accepted 15th August 2017

DOI: 10.1039/c7ra05955h

rsc.li/rsc-advances

Manganese oxides have been proven to be promising adsorbents to capture Pb(II) from wastewaters. In nature, MnO_2 can be found in different crystalline structures, while the effect of crystal structure on their adsorption performance remains unclear. In this study, five manganese oxides with different crystallographic phases, α-, β-, γ-, δ-, and λ-MnO_2 were prepared and characterized by X-ray diffraction (XRD), transmission electron microscopy (TEM), X-ray photoelectron spectroscopy (XPS), N_2 adsorption–desorption, Fourier transform infrared (FT-IR) spectroscopy and zeta potential measurements. The adsorptive removal of aqueous Pb(II) was investigated using these manganese oxides as adsorbents. The results showed that the adsorption capacities of manganese oxides for Pb(II) varied with BET surface area and crystalline structure, following the order of δ-MnO_2 > α-MnO_2 > λ-MnO_2 > γ-MnO_2 > β-MnO_2. δ-MnO_2 displayed the highest capacity for Pb(II), and the adsorption was scarcely influenced by the presence of the coexisting Na^+ cation. The surface complexation model was used to describe the Pb(II) adsorption on the MnO_2 adsorbents. In a column adsorption test δ-MnO_2 was capable of continuously treating 25 000 bed volumes synthetic wastewater stream with an influent concentration of 20 mg L^{-1} Pb(II) and an effluent concentration below 0.5 mg L^{-1}. This work indicates that δ-MnO_2 has great potential to be used as an effective adsorbent for Pb(II) removal.

1. Introduction

Water pollution by Pb(II) is a serious environmental problem. Wastewaters from various industrial activities usually contain considerable amounts of Pb(II) which can be a severe threat to public health.[1] Toxicity studies have demonstrated that Pb(II) can be accumulated in human body because of its high volatility and non-biodegradability, causing neurological, reproductive and immunological pathologies.[2,3] Therefore, a simple and cost-effective treatment technique to remove Pb(II) from the environment is recognized as a top priority by the World Health Organization (WHO).[4]

Adsorption is considered as an effective and economic technology to remove Pb(II) from water prior to its discharge into the natural environment. A variety of materials have been explored for adsorptive removal of Pb(II) from water, including carbon materials,[5] clay minerals[6,7] and metal oxides (*e.g.* Fe_2O_3, Al_2O_3 and MnO_2),[8] and MnO_2 was found to be the one of the most active species for Pb(II) removal.[9] Wang *et al.*[10] prepared layered birnessite type MnO_2 and found that the adsorbent was effective for the removal of Pb(II) at pH 4.5. In parallel, Maliyekkal *et al.* synthesized cellulose–manganese oxide hybrid material for adsorptive removal of Pb(II) in water.[11] It should be emphasized that manganese oxides are suitable for Pb(II) adsorption because of the high specific surface area, low isoelectric point (IEP) and negatively charged surface over a wide pH range.[12] Tonkin *et al.*[13] reported that Pb(II) could be effectively adsorbed on δ-MnO_2 within the pH range of 2–9. Moreover, manganese oxides have attracted special attention because of their outstanding structural flexibility, low-cost and environmental friendliness, which have been widely applied in adsorbents,[9] catalysts[14] and cathodes.[15]

Manganese oxides are widely used in adsorption of removing Pb(II) from aqueous solutions. However, according to some recent studies, the adsorption affinity of MnO_2 towards Pb(II) was highly related to the structures and surface properties of MnO_2. Luo *et al.*[16] studied adsorptive removal of lithium by 3D-MnO_2 from wastewater and found that 3D-MnO_2 with high degree of porosity and large pores exhibited a higher adsorption capacity than 1D-MnO_2. Kozlova *et al.*[17] prepared complex manganese oxides with different sizes of structural tunnels, and concluded that the tunnel size was the determining factor for the sorption of heavy metal cations. In addition, Korshin *et al.*[18] and Abdullah *et al.*[19] found that heavy metal ions could be complexed at different adsorption sites on birnessite and α-MnO_2 using EXAFS spectroscopy. Wang *et al.*[10] studied the adsorption mechanisms of Pb(II) onto varied birnessite type

State Key Laboratory of Pollution Control and Resource Reuse, Jiangsu Key Laboratory of Vehicle Emissions Control, School of the Environment, Nanjing University, Nanjing 210023, China. E-mail: zhaoyixu@nju.edu.cn; Fax: +86-25-89680596; Tel: +86-25-89680370

MnO_2 and found that the adsorption capacities were largely controlled by the Mn average oxidation states and type of sorption sites on the MnO_2 surface. Notably, MnO_2 exists in five main crystallographic forms in nature: α-, β-, γ-, δ-, and λ- types, as the basic structure unit, [MnO_6] octahedron, links in different conditions.[20] The crystalline structures are generally believed to be responsible for their chemical and physical properties.[21] The influence of crystal forms on MnO_2 catalytic performance has been extensively studied.[22,23] Different crystallographic MnO_2 materials were also prepared for pollutants adsorption, and MnO_2 adsorbents showed varying adsorption performance depending on the surface area and crystalline structure. Zhang *et al.* investigated the effect of the crystallographic structure of MnO_2 on Li^+ adsorption, and found that MnO_2 ion sieve with λ-crystallographic structure exhibited higher capacity for Li(I) selective adsorption.[24] Kanungo and Parida prepared MnO_2 adsorbents with different crystallographic forms (α-, β-, γ- and δ-MnO_2), and adsorption of Cu(II) on those adsorbents were studied. They found the layered δ-MnO_2 showed the highest adsorption capacity and the adsorption capacity was directly related to BET surface area.[25] To gain a better understanding of the effect of MnO_2 structure on adsorption behaviors, the adsorption comparison of Pb(II) on α-, β-, γ-, δ-, and λ-MnO_2 were made in our experiments. However, to the best of our knowledge, no attempt has been made.

In this study, α-, β-, γ-, δ-, and λ-MnO_2 were prepared and characterized by X-ray diffraction (XRD), X-ray photoelectron spectroscopy (XPS), transmission electron microscopy (TEM), Fourier transform infrared (FT-IR), N_2 adsorption/desorption and zeta potential measurements. The adsorption properties of the adsorbents toward Pb(II) in aqueous solution were systematically examined for adsorption capacity and effect of water chemistry. The influence of crystal forms of MnO_2 on their adsorption performance was investigated in conjunction with important physicochemical parameters. Column adsorption tests were also carried out to elucidate the applicability of δ-MnO_2 in Pb(II) removal from synthetic wastewater effluent.

2. Experimental section

2.1 Materials and reagents

Chemicals used in the experiments were of analytical grade and were used without further purification. All chemicals including manganese sulfate ($MnSO_4 \cdot H_2O$), ammonium persulfate ($(NH_4)_2S_2O_8$), potassium hypermanganate ($KMnO_4$), lead nitrate ($Pb(NO_3)_2$), sodium nitrate ($NaNO_3$), magnesium nitrate ($Mg(NO_3)_2$), calcium nitrate ($Ca(NO_3)_2$) were purchased from Nanjing Chemical Reagents Co., Ltd. Stock solutions of Pb(II) was prepared by dissolving appropriate amount of $Pb(NO_3)_2$ in deionized (DI) water.

2.2 Preparation of manganese oxides

The α-MnO_2, β-MnO_2, and γ-MnO_2 were prepared by the hydrothermal method according to the literature.[20] In brief, 2.4 g of $MnSO_4 \cdot H_2O$ and appropriate amount of $(NH_4)_2S_2O_8$ (5.3 g for α-MnO_2, and 3.7 g for β-MnO_2 and γ-MnO_2) were put into DI water at room temperature to form a homogeneous solution, which was then transferred into a 40 mL Teflon-lined stainless steel autoclave and heated for 12 h. The hydrothermal temperature was set at 90 °C for γ-MnO_2, and 140 °C for α-MnO_2 and β-MnO_2. After the reaction was completed, the resulting solid product was filtered and washed with DI water, drying at 110 °C for 12 h.

To prepare δ-MnO_2, 1.8 g of $KMnO_4$ was dissolved in 100 mL DI water, then 30 mL H_2O_2 (30%) was added dropwise to the solution under fast stirring. The solution pH was kept at 7.0 ± 0.2 using 0.1 mol L^{-1} HNO_3 and/or KOH. After continuously stirring for another 30 min, the suspension was aged at room temperature for 3 h. Then the aged precipitate was filtered and washed with DI water and dried at 110 °C for 12 h.

The λ-MnO_2 was prepared using $LiMn_2O_4$ as the precursor. Four grams of $KMnO_4$, 1.5 g of NaCl and 4.5 g of LiCl were grinded thoroughly and transferred to ceramic crucible, followed by a heat-treatment at 600 °C for 5 h.[26] The resulting solid product was added in 200 mL 0.1 mol L^{-1} HNO_3 solution under fast stirring for 12 h. After the acid treatment, the suspension was filtered and the solid product was washed with DI water and dried at 110 °C for 12 h.

2.3 Characterization of manganese oxides

Powder XRD patterns of the samples were collected on a Rigaku D/max-RA powder diffraction meter with Cu Kα radiation (Rigaku, Japan). TEM images of the samples were collected on a Hitachi H-800 transmission electron microscope (Hitachi, Japan). The specific surface areas of the adsorbents were measured by N_2 adsorption/desorption after pretreated at 200 °C under vacuum (1.33 Pa) for 4 h on a Micrometrics ASAP 2020 analyzer (Micromeritics ASAP 2020, USA) at −196 °C (77 K) and were calculated by the Brunauer–Emmett–Teller (BET) method. FT-IR spectra of the samples were recorded on a Nicolet Nexus 870 FT-IR spectrometer (Nicolet, USA) with the KBr pellet technique. An XPS spectrometer (Perkin Elmer PHI 550 ESCA/SAM, USA) equipped with a monochromatized Al Kα X-ray source ($h\nu$ = 1486.6 eV) and a hemispherical electron analyzer was used to analyze the surface properties of the samples. The C 1s peak (284.6 eV) was used for the calibration of binding energy values. Surface zeta potentials (ζ) of the materials were measured using a zeta potential analyzer (Zeta PALS, Brookhaven Instruments Co., USA). Briefly, 0.01 g of materials were dispersed in 100 mL of 1 mmol L^{-1} NaCl with varied pH adjusted using 0.1 mol L^{-1} HCl or NaOH, and the suspension was allowed to settle for 24 h before zeta-potential measurement.

2.4 Adsorption kinetics

To examine the adsorption kinetic of Pb(II) to the adsorbent, 0.25 g of adsorbent was added into a 500 mL round-bottom flasks containing 500 mL of Pb(II) solution with varied initial concentrations under vigorous magnetic stirring. The initial Pb(II) concentrations were 45.0 mg L^{-1} for α-, β-, γ- and λ-MnO_2, and 150.0 mg L^{-1} for δ-MnO_2. The samples were taken from the flasks at preset time intervals and the adsorbent was removed

by fast filtration. The concentration of Pb(II) in the filtrate was determined by AAS, and the adsorption amount was calculated according to the following equation:

$$q_t = \frac{(C_0 - C_t)V}{M} \quad (1)$$

where q_t (mg g^{-1}) is the adsorption amount at time t, C_0 (mg L^{-1}) is the initial concentration of Pb(II) in solution, C_t (mg L^{-1}) is Pb(II) concentration at time t, V (L) is the solution volume, and M (g) is the mass of the adsorbent.

2.5 Adsorption isotherms

Adsorption isotherms of Pb(II) on the adsorbents were obtained from batch experiments by placing 20.0 mg of adsorbent in 40 mL polytetrafluoroethylene-lined screw cap glass tubules receiving 40 mL of $Pb(NO_3)_2$ aqueous solutions with varied initial concentrations. The pH of the aqueous solutions was adjusted to 4.0 ± 0.2 using 0.1 mol L^{-1} HNO_3 or NaOH. Then, the samples were shaken at room temperature for 24 h in an orbital shaker. The time period was sufficient to reach apparent adsorption equilibrium based on preliminarily determined adsorption kinetics. After shaking, the sample was filtrated using a 0.45 μm filter, and Pb(II) concentration in the was filtrate determined by AAS. The adsorbed amount of Pb(II) at equilibrium was calculated according to the following equation:

$$q_e = \frac{(C_0 - C_e)V}{M} \quad (2)$$

where q_e (mg g^{-1}) and C_e (mg L^{-1}) are the adsorbed concentration and aqueous concentration of Pb(II) at equilibrium, respectively, C_0 (mg L^{-1}) is the initial Pb(II) concentration, V (L) is the solution volume, and M (g) is the adsorbent mass.

The impact of ionic strength and pH on Pb(II) adsorption was tested in the presence of $NaNO_3$ solutions with varied concentrations (0.001, 0.01, and 0.10 mol L^{-1}) in a pH range of 2.5–10.0. The initial Pb(II) concentrations were 45.0 mg L^{-1} for α-, β-, γ- and λ-MnO_2, and 150.0 mg L^{-1} for δ-MnO_2. The initial pH of Pb(II) solution was adjusted using 0.1 mol L^{-1} HNO_3 or NaOH, and the pH of all samples was measured after adsorption equilibrium. All adsorption experiments were conducted in duplicate.

2.6 Fixed-bed column adsorption

The experiments of column adsorption were carried out in a polyethylene column (1.78 mm internal diameter, 130 mm in length) equipped at room temperature. The wet δ-MnO_2 (bed volume = 2.0 mL, M = 3.27 g) or silica sand was packed within the columns before operation. A control of only silica sand was also tested and the results revealed that the silica sand did not adsorb Pb(II) (data not shown). A synthetic influent solution containing Pb(II) (20.0 mg L^{-1}), Na(I) (100.0 mg L^{-1}), Mg(II) (100.0 mg L^{-1}) and Ca(II) (150.0 mg L^{-1}) was pumped upflow through the column at flow rate of 15.0 mL h^{-1} using a Lange-580 pump (Baoding, China). The effluent was collected regularly by a BSZ-100 programmable fraction collector (Shanghai, China) and measured by AAS. As for the regeneration test, a mixed solution containing 0.1 mol L^{-1} HNO_3 and 5 wt% $Ca(NO_3)_2$ was used as the regenerant and the flow rate was 7.5 mL h^{-1}.

3. Results and discussion

3.1 Characterization of adsorbents

The XRD patterns of varied MnO_2 adsorbents are compiled in Fig. 1. For α-MnO_2, diffraction peaks were identified with 2θ at 22.5°, 28.7°, 37.5°, 42.0°, 49.9°, 56.6°, 59.9°, 65.3° and 68.9°, indicative of the presence of manganese oxide with a tetragonal structure.[20] As for β-MnO_2, diffraction peaks were observed with 2θ at 28.6°, 37.3°, 40.9°, 42.8°, 46.1°, 56.7°, 59.3° and 64.9°, assigned to rutile structure.[20] The XRD pattern of γ-MnO_2 displayed four distinct diffraction peaks at 22.2°, 37.6°, 42.5° and 56.2°, corresponding to manganese oxide resulted from a random intergrowth of blocks of the rutile-type structural units within the Ramsdellite structure.[20] Two low intensity and broad diffraction peaks at 37.0° and 67.5° were observed for δ-MnO_2, characteristic of hexagonal randomly-stacked and single phased birnessite-type MnO_2.[27] The diffraction peaks of λ-MnO_2 were identified with 2θ at 36.5°, 38.2°, 44.4°, 48.8°, 58.9°, 64.6°, 65.6° and 67.9°, indicative of cubic spinel structure for λ-MnO_2.[26] The XRD results clearly revealed the successful preparation of varied MnO_2 crystallographic forms.

The TEM images of the five MnO_2 adsorbents are compared in Fig. 2 α-MnO_2 (Fig. 2a) was shown to be ribbon-like nanowires with diameters around 10 nm and lengths ranging between 0.06 and 0.4 μm. β-MnO_2 (Fig. 2b) and γ-MnO_2 (Fig. 2c) were observed to be nanorods with average diameters of 100 and 20 nm, respectively. As for δ-MnO_2 (Fig. 2d), the layered structure was clearly identified, which was commonly formed by MnO_2 nanosheets organizing in layer-by-layer structure for multilayer systems. The λ-MnO_2 (Fig. 2e) had a cubic structure with a size about 20 nm, which was consistent with the XRD results. The BET surface areas were 97.5, 14.2, 71.4, 270.8 and 36.6 for α-, β-, γ-, δ-, and λ-MnO_2, respectively. The δ-MnO_2 with a layered structure exhibited a highest BET surface area, which was likely because the layer spacing of δ-MnO_2 was large enough

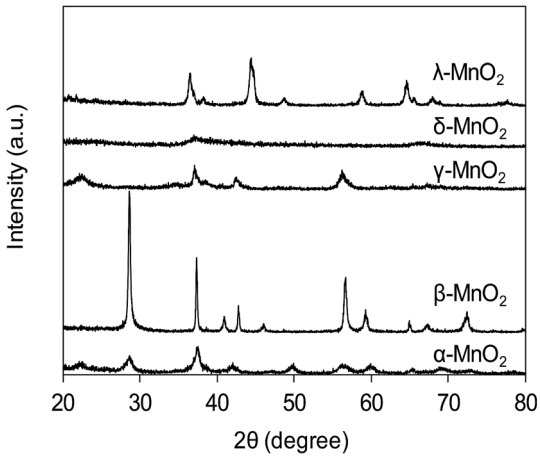

Fig. 1 XRD patterns of synthetic MnO_2 samples.

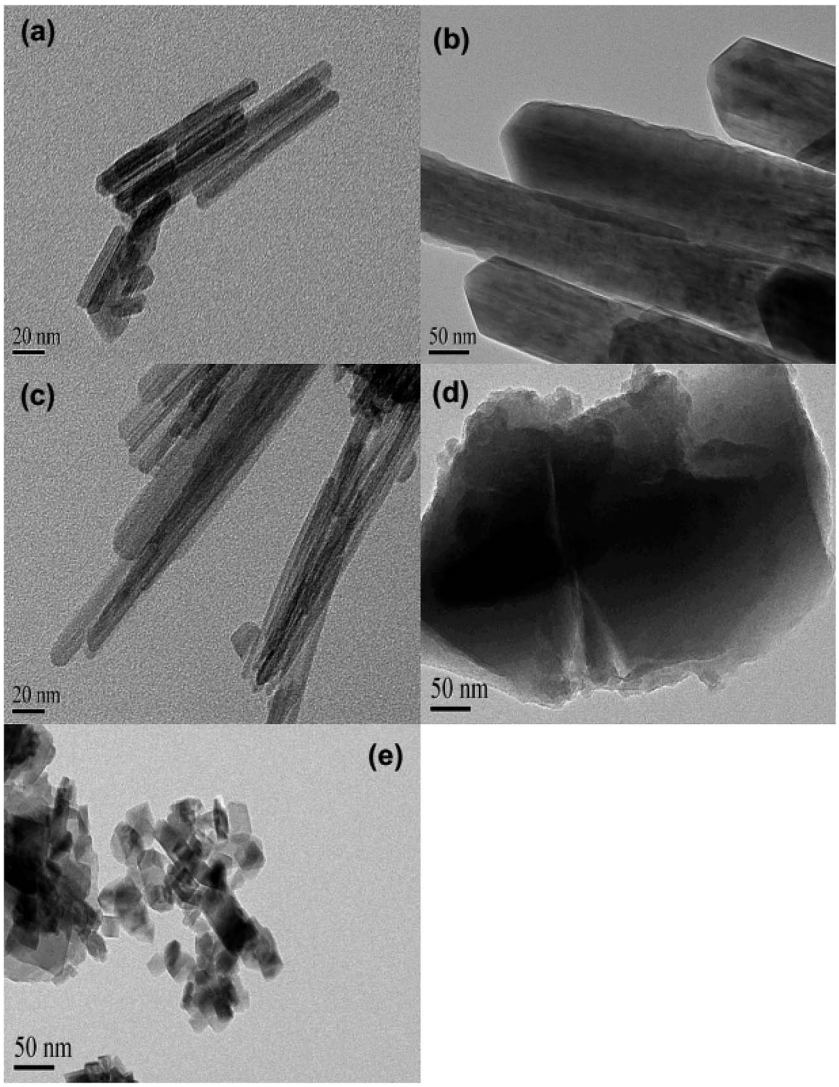

Fig. 2 TEM images of (a) α-MnO_2, (b) β-MnO_2, (c) γ-MnO_2, (d) δ-MnO_2, and (e) λ-MnO_2.

to host N_2 molecules. As for α-, β-, γ- and λ-MnO_2, N_2 molecules were mainly adsorbed on the external surface.[23]

The XPS spectra of the adsorbents in the Mn $2p_{3/2}$ and O 1s regions are compared in Fig. 3a and b, respectively. As can be seen in Fig. 3a, the Mn $2p_{3/2}$ spectrums were asymmetrical and could be divided into three peaks at 639.9, 641.2 and 642.2 eV, assigned to Mn^{2+}, Mn^{3+} and Mn^{4+}, respectively.[10,28] To obtain the relative quantity of Mn^{2+}, Mn^{3+} and Mn^{4+} in the adsorbents, the Mn $2p_{3/2}$ spectrums were fitted according to the literature,[10,29] and the fitting results are listed in Table 1. The content of Mn^{3+} in α- and β-MnO_2 were higher than others. According to literature, the higher Mn^{3+} content led to fewer cationic vacancies because the Mn^{3+} site binding might involve additional complexes when compared to Mn^{4+}.[10] The O 1s spectrums (Fig. 3b) of the adsorbents were highly asymmetrical and were divided into two peaks at 528.6–529.0 eV and 530.9–531.0 eV, assigned to oxygen containing species of lattice oxygen and adsorbed oxygen, respectively.[30] The contents of lattice oxygen and adsorbed oxygen in the adsorbents are listed in Table 1. As for δ-MnO_2, the content of adsorbed oxygen was the highest among the adsorbents, revealing an abundance of surface hydroxyl groups.

The functional groups on MnO_2 surface were studied by FT-IR, and the FT-IR spectra of the adsorbents are compiled in Fig. 4. The broad band appearing at around 3400 cm^{-1} was assigned to O–H stretching and the band at 1610 cm^{-1} was attributed to O–H bending vibration.[31] For all MnO_2 adsorbents, the characteristic bands at 400–800 cm^{-1} were observed, corresponding to the Mn–O lattice vibration.[27] For the layered δ-MnO_2 and cubic spinel λ-MnO_2, the bands around 416, 441 and 512 cm^{-1} were recorded, which is in good agreement with reported FT-IR characteristic bands in literature.[27] However, as for the tunnel α-, β- and γ-MnO_2 the position of those characteristic bands displayed some obvious changes. A weak band around 711 cm^{-1} was observed, corresponding to the manganese oxides with tunnel structure.[32,33] Additionally, the band at 1106 cm^{-1} was also recorded in the FT-IR spectra of α- and γ-MnO_2, characteristic of the vibration of the Mn^{3+}–O bond.[27]

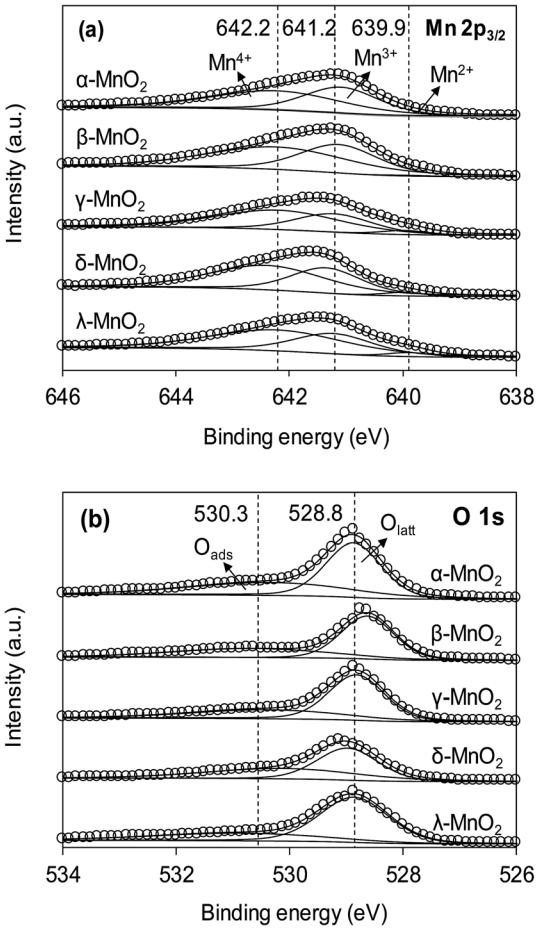

Fig. 3 (a) Mn $2p_{3/2}$ and (b) O 1s XPS spectra of different MnO_2 adsorbents.

This observation suggests that some Mn^{3+} occupies the Mn^{4+} sites in the frameworks of α- and γ-MnO_2. These results implied that the crystal structure of MnO_2 played a key role in affecting the Mn–O lattice vibration as well as the nature of surface hydroxyl groups.

Surface zeta potentials of the varied crystallographic MnO_2 as a function of solution pH are compared in Fig. 5. Within the test pH range, surface zeta potentials of all adsorbents monotonically decreased due to the continuous deprotonation effect

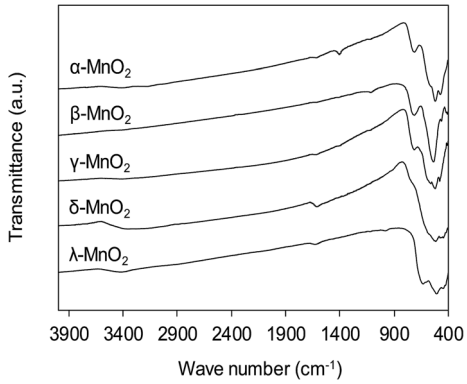

Fig. 4 FT-IR spectra of MnO_2 adsorbents with different crystallographic forms.

of surface hydroxyl groups. The isoelectric points (IEP) of α-, β-, γ-, δ-, and λ-MnO_2 were found to be 2.4, 2.4, 2.0, 1.3 and 2.6, respectively, similar to those reported in literatures.[12,21,26,34] Additionally, negative surface zeta potentials were observed on the five adsorbents over a wide pH range, suggesting the potential for adsorptive removal of Pb(II) in water. Notably, much lower ζ potential was observed in δ-MnO_2 than in others in the test pH range of 1.0–6.0.

3.2 Adsorption kinetics

Fig. 6a compares the kinetics of Pb(II) adsorption onto the five MnO_2 adsorbents. It was shown that the adsorption of Pb(II) on MnO_2 adsorbents were very fast. The Pb(II) adsorption amounts increased sharply within 20 min and reached equilibrium at about 150 min. The kinetic data were fitted using the pseudo-second-order kinetic model as follow:[21]

$$\frac{t}{q_t} = \frac{1}{kq_e^2} + \frac{t}{q_e} \tag{3}$$

where q_e (mg g^{-1}) and q_t (mg g^{-1}) are the adsorbed amount at equilibrium and time t (min), respectively, and k (g mg^{-1} min^{-1}) is the pseudo-second-order rate constant. Fig. 6b displays the linear fitting plots of Pb(II) adsorption on the adsorbents to the pseudo-second-order kinetics. The fitting parameters are summarized in Table 2. High correlation coefficients (R^2 > 0.99) and the consistence of calculated q_{cal} values with experimental data indicated

Table 1 The results of XPS Mn $2p_{3/2}$ and O 1s multiplets peak fitting

	Mn^{4+}			Mn^{3+}			Mn^{2+}			O_{latt}			OH_{ads}		
Sorbents	BE[a] (eV)	FWHM[b] (eV)	At.[c] (%)	BE (eV)	FWHM (eV)	At. (%)	BE (eV)	FWHM (eV)	At. (%)	BE (eV)	FWHM (eV)	At. (%)	BE (eV)	FWHM (eV)	At. (%)
α-MnO_2	642.22	2.72	56.1	641.08	1.57	43.9	639.02	1.18	0.0	528.62	1.10	61.7	530.67	3.29	38.3
β-MnO_2	642.21	2.93	58.3	641.13	1.62	41.1	639.91	0.91	0.6	528.87	1.15	58.9	530.31	3.40	41.1
γ-MnO_2	642.18	2.64	60.1	641.21	1.61	35.2	639.96	0.96	4.7	528.82	1.15	64.0	530.37	3.17	36.0
δ-MnO_2	642.29	2.38	58.9	641.35	1.46	38.1	639.99	0.85	3.0	528.97	1.26	55.7	530.10	3.20	44.3
λ-MnO_2	642.21	2.78	60.5	641.22	1.63	35.6	639.87	0.90	3.9	528.86	1.43	71.0	530.86	3.53	29.0

[a] Binding energy. [b] The FWHM of all peaks were constrained. [c] At. represents the percentage of the contribution for each peak to the total number of counts under the Mn $2p_{3/2}$ or O 1s peak, and all peaks modeled as 70% Gaussian–30% Lorentzian.

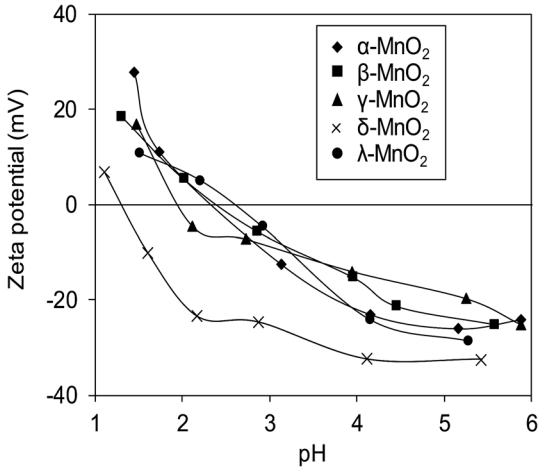

Fig. 5 Zeta potential of different MnO_2 adsorbents as a function of pH.

that Pb(II) uptake onto the adsorbents could be described by the pseudo-second-order kinetic model and were controlled by chemisorption rather than mass transport.[21] The adsorption rates of Pb(II) adsorption on the adsorbents were in the order of γ-MnO_2 > α-MnO_2 > β-MnO_2 > λ-MnO_2 > δ-MnO_2, reflecting a lower adsorption kinetic on layered MnO_2 adsorbent.

To further verify the controlling mechanism involved in the adsorption process, Weber–Morris model was used to fit the kinetic adsorption data. The model is expressed as follows:[21]

$$q_t = k_i t^{1/2} + C_i \quad (4)$$

where k_i (mg g^{-1} $min^{-1/2}$) is the intraparticle diffusion rate constant, and C_i is the intercept.

Fig. 6c presents the plots of q_t *versus* $t^{1/2}$ for adsorption of Pb(II) onto the five adsorbents, and the fitting parameters are listed in Table 2. The q_t–$t^{1/2}$ relations clearly exhibited multi-linearity, reflecting that the adsorption process appeared to be controlled by more than one step. According to Weber–Morris model, the adsorption process is only controlled by intraparticle diffusion when $C_i = 0$. For δ-MnO_2, the q_t–$t^{1/2}$ plots consisted of three linear portions, and the first linear portion did not pass through the origin, suggesting the involvement of external diffusion.[21] Therefore, the first linear portion was attributed to the fast lead adsorption onto δ-MnO_2 external surface and the second one was indicative of Pb(II) diffusion into the interlayer space of the adsorbent, and the third one was characteristic of the final equilibrium step. Notably, the majority of Pb(II) adsorption onto δ-MnO_2 was observed in second linear portion and the intraparticle diffusion was slower than the external surface diffusion. In contrast, the Weber–Morris plots of α-, β-, γ- and λ-MnO_2 consisted of two linear portions, in which the first linear portion was Pb(II) diffusion to the sorbents external surfaces and the second one was the final equilibrium stage.

3.3 Adsorption isotherms

The adsorption isotherms of Pb(II) onto various MnO_2 adsorbents are compared in Fig. 7a. For δ-MnO_2, Pb(II) adsorption

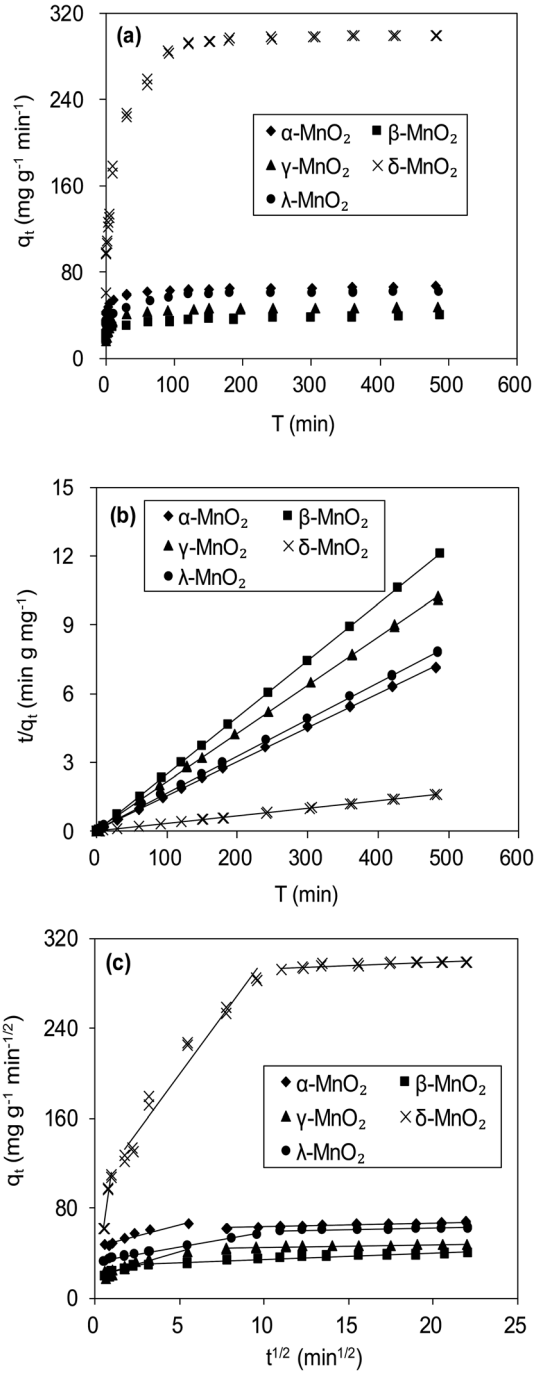

Fig. 6 (a) Time resolved Pb(II) adsorption on MnO_2 adsorbents, and fitting of Pb(II) adsorption kinetics using (b) pseudo second-order model and (c) Weber–Morris model. The initial Pb(II) concentrations were 45.0 mg L^{-1} for α-, β-, γ- and λ-MnO_2, and 150.0 mg L^{-1} for δ-MnO_2.

amount was 242.6 mg g^{-1} at an equilibrium concentration of 28.2 mg L^{-1}, which was significantly larger than that for α-, β-, γ- and λ-MnO_2 (84.4, 58.9, 62.1 and 61.9 mg g^{-1}, respectively). To analyze the adsorption behavior of the adsorbents, the adsorption isotherms were further modeled using Langmuir and Freundlich models. The Langmuir isotherm model is expressed as follows:

Table 2 Fitting parameters of Pb(II) adsorption kinetics to MnO_2 adsorbents using pseudo second-order and Weber–Morris model

		Pseudo second-order			Weber–Morris model					
Sorbents	q_{exp}, mg g^{-1}	k, mg g^{-1} min^{-1}	q_{cal}, mg g^{-1}	R^2	k_1, mg g^{-1} min$^{-1/2}$	C_1	R^2	k_2, mg g^{-1} min$^{-1/2}$	C_2	R^2
α-MnO_2	67.6	4.40×10^{-3}	67.1	0.99	3.63	40.75	0.94			
β-MnO_2	40.3	3.42×10^{-3}	39.7	0.99	3.78	18.82	0.85			
γ-MnO_2	47.9	5.94×10^{-3}	47.6	0.99	4.44	18.42	0.90			
δ-MnO_2	299.2	6.07×10^{-4}	303.0	0.99	36.67	1.65	0.92	20.51	97.27	0.96
λ-MnO_2	62.4	3.31×10^{-3}	62.5	0.99	2.59	32.33	0.99			

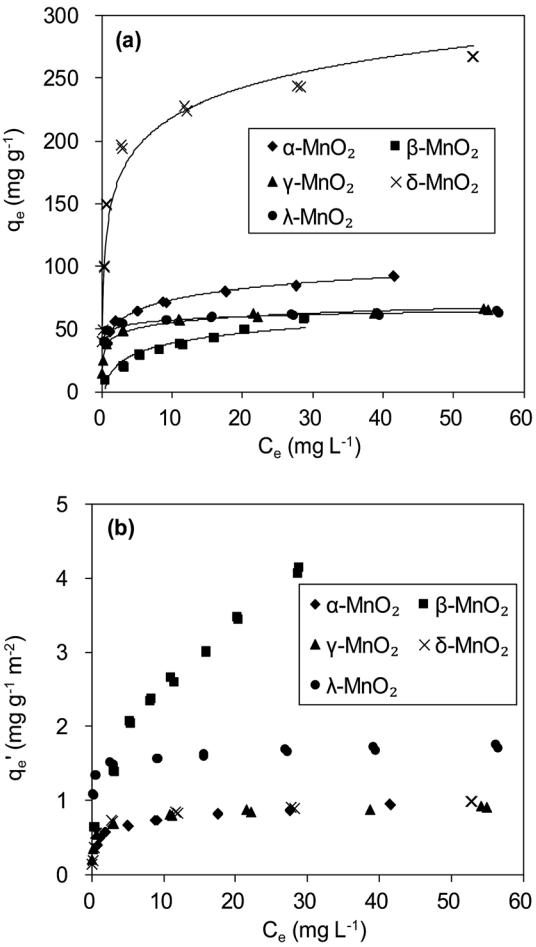

Fig. 7 (a) Pb(II) adsorption isotherms and (b) BET surface area normalized Pb(II) adsorption isotherms on MnO_2 adsorbents.

$$\frac{C_e}{q_e} = \frac{1}{q_m b} + \frac{C_e}{q_m} \quad (5)$$

where q_m (mg g^{-1}) is the maximum adsorption capacity, and b (L mg^{-1}) is the Langmuir equilibrium constant.

The Freundlich isotherm model can be described as:

$$\log q_e = \log K_f + \frac{1}{n} \log(C_e) \quad (6)$$

where K_f is Freundlich coefficient that characterizes the adsorption capacity of the adsorbent, and n is the linearity index which reflects the intensity of adsorption.

The fitting parameters are summarized in Table 3. High correlation coefficients (R^2) were achieved for the Langmuir and Freundlich models, indicating that Pb(II) adsorption onto the adsorbents could be well described by these two models. The maximum adsorption capacity q_m value and Freundlich coefficient K_f value for δ-MnO_2 were both higher in comparison with the other MnO_2, confirming the largest adsorption capacity of δ-MnO_2. This can be explained by different BET surface area of the five MnO_2 adsorbents. Among the five MnO_2 adsorbents, δ-MnO_2 exhibited the largest BET surface area with abundant hydroxyl groups as observed in XPS and FT-IR spectra.[30] Compared with the other three MnO_2 adsorbents, γ- and λ-MnO_2 had larger b values in Langmuir model, suggesting their high affinity for Pb(II). This is likely due to the high contents of Mn^{4+} in γ- and λ-MnO_2. The charge imbalance on Mn^{4+} sites is much higher than on Mn^{3+} and Mn^{2+} sites and the former sites exhibit higher affinity for metal binding. Thus, structural forms of MnO_2 had great impact on its Pb(II) adsorption performance.

The interaction of Pb(II) with surface hydroxyl groups was confirmed by the XPS results of MnO_2 after Pb(II) adsorption. Fig. 8 displays the XPS spectra of Pb 4f and O 1s of the MnO_2 after Pb(II) adsorption. The MnO_2 adsorbents displayed two peaks with Pb $4f_{7/2}$ and Pb $4f_{5/2}$ derived from spin–orbit splitting. The binding energy of Pb $4f_{7/2}$ core level was observed at around 138.6 eV, reflecting the orthorhombic PbO compound and no hydroxides or carbonates precipitation of Pb during adsorption.[21] As for O 1s spectra, after Pb(II) adsorption the ratio of O_{ads} decreased in all MnO_2 adsorbents. This was likely due to the complexation interactions between surface –OH and Pb(II). The increase of O_{latt} ratio in Pb(II)-loaded MnO_2 was attributed to the formation of Pb–O–Mn bond and the higher binding energy of O 1s in Pb(II)-loaded MnO_2 confirmed the covalent of Pb–O–Mn linkage.

More insight into the structural properties of the adsorbents with varied crystallographic forms could be gained by comparing the surface area normalized adsorption isotherms, and the results are shown in Fig. 7b. Among the tested adsorbents, the normalized adsorption capacity of β-MnO_2 was much higher. This could be well explained by the interface reaction mechanism inferred from adsorbate–adsorbent polyhedral linkage. Previous studies found that the [MnO_6] octahedral structure units of the manganese dioxide were connected with the edge and double-corner linkages, and concluded that Pb(II) was adsorbed at double-corner-sharing (DCS) and double-edge-

Table 3 Parameters of Langmuir and Freundlich isotherm model for the adsorption of Pb(II) onto sorbents

	Langmuir model			Freundlich model		
Sorbents	b (L g^{-1})	q_m (mg g^{-1})	R^2	K_f (mg^{1-n} L^{-1} g^{-1})	n	R^2
α-MnO_2	1.08	84.0	0.97	45.4	5.08	0.96
β-MnO_2	0.55	42.4	0.93	12.5	2.20	0.99
γ-MnO_2	12.93	51.6	0.92	34.6	5.35	0.94
δ-MnO_2	3.57	200.0	0.92	112.2	3.68	0.87
λ-MnO_2	6.92	60.2	0.96	47.5	13.02	0.91

sharing (DES) sites.[35] Notably, β- and λ-MnO_2 is composed of single strands of edge-sharing [MnO_6] octahedral with 1 × 1 tunnels, while α- and γ-MnO_2 are constructed from the chains of 2 × 2, 1 × 1 and 1 × 2 tunnels, respectively.[20,36] Thus, more DCS and DES adsorption sites per unit area were observed on β- and λ-MnO_2 surfaces, making them showed higher surface area normalized adsorption capacities of Pb(II). Additionally, δ-MnO_2 exhibited nearly identical normalized adsorption capacity to that of α- and γ-MnO_2. These results further implied that crystal structure confinement effect was the main factor that affected the adsorption capacity.

The q_m value for δ-MnO_2 (200.0 mg g^{-1}) synthesized in this study was also markedly larger than the values reported for many other adsorbents such as coconut shell carbon (26.5 mg g^{-1}),[37] amino-functionalized Fe_3O_4@SiO_2 (76.7 mg g^{-1}),[38] montmorillonite (158.5 mg g^{-1})[7] and nanoscale organo-functionalized SiO_2–Al_2O_3 (183.0 mg g^{-1}).[39] Hence, the δ-MnO_2 exhibited a significantly higher adsorption capacity than these other adsorbents. Additionally, the synthesis cost of δ-MnO_2 was much less than amino-functionalized Fe_3O_4@SiO_2, which was feasible for industrial Pb(II) recycling.

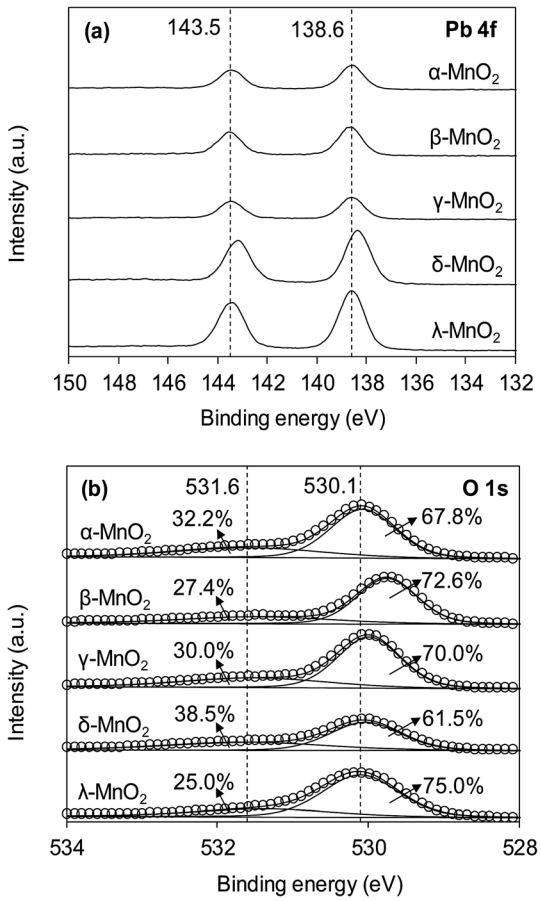

Fig. 8 (a) Pb 4f and (b) O 1s XPS spectra of MnO_2 adsorbents after Pb(II) adsorption.

3.4 Effect of pH and ionic strength

The effects of pH and ionic strength on Pb(II) adsorption to the adsorbents were examined, and the results are presented in Fig. 9. For the five adsorbents, Pb(II) adsorption was significantly affected by the solution pH, which increased continuously in the experimental pH range of 2.5–5.5. It should be noted that Pb(II) would precipitate under high pH (*e.g.* pH > 7.0) conditions. The effect of pH on Pb(II) adsorption on MnO_2 could be well explained by the electrostatic interaction mechanism. Because surface hydroxyl groups were the adsorption sites, the impact of solution pH on Pb(II) adsorption predominantly depending on the protonation–deprotonation transition of surface hydroxyl groups.[13,21] The results of zeta potential showed that the isoelectric points (IEP) of α-, β-, γ-, δ-, and λ-MnO_2 were found to be 2.4, 2.4, 2.0, 1.3 and 2.6, respectively, indicated that MnO_2 was negatively charged at pH values above the IEP and electrostatic attractive interaction was expected at high pH, resulting in increased Pb(II) adsorption. When the solution pH values below IEP, MnO_2 was positively charged and repulsive interaction occurred at low pH between Pb(II) and MnO_2, thus displaying lowered Pb(II) adsorption. The ζ potential analysis showed that MnO_2 surface became more negative charged with increasing solution pH, which would enhance the attraction of Pb(II). The nearly negligible Pb(II) adsorption on the sorbents at pH 2.0 suggested that the saturated adsorbent could be regenerated under acidic conditions.

In $NaNO_3$ solutions, the formation of aqueous Pb(II) complexes with NO_3^- and OH^- species might affect the Pb(II) adsorption on MnO_2 as reported in previous work.[41] The aqueous speciation reactions of Pb(II) with the electrolyte anions (OH^- and NO_3^-) were described as follows:[40,41]

$$Pb^{2+} + H_2O = Pb(OH)^+ + H^+, \log K = -6.19 \quad (7)$$

$$Pb^{2+} + 2H_2O = Pb(OH)_2(s) + 2H^+, \log K = -8.15 \quad (8)$$

$$Pb^{2+} + NO_3^- = PbNO_3^+, \log K = 1.1 \quad (9)$$

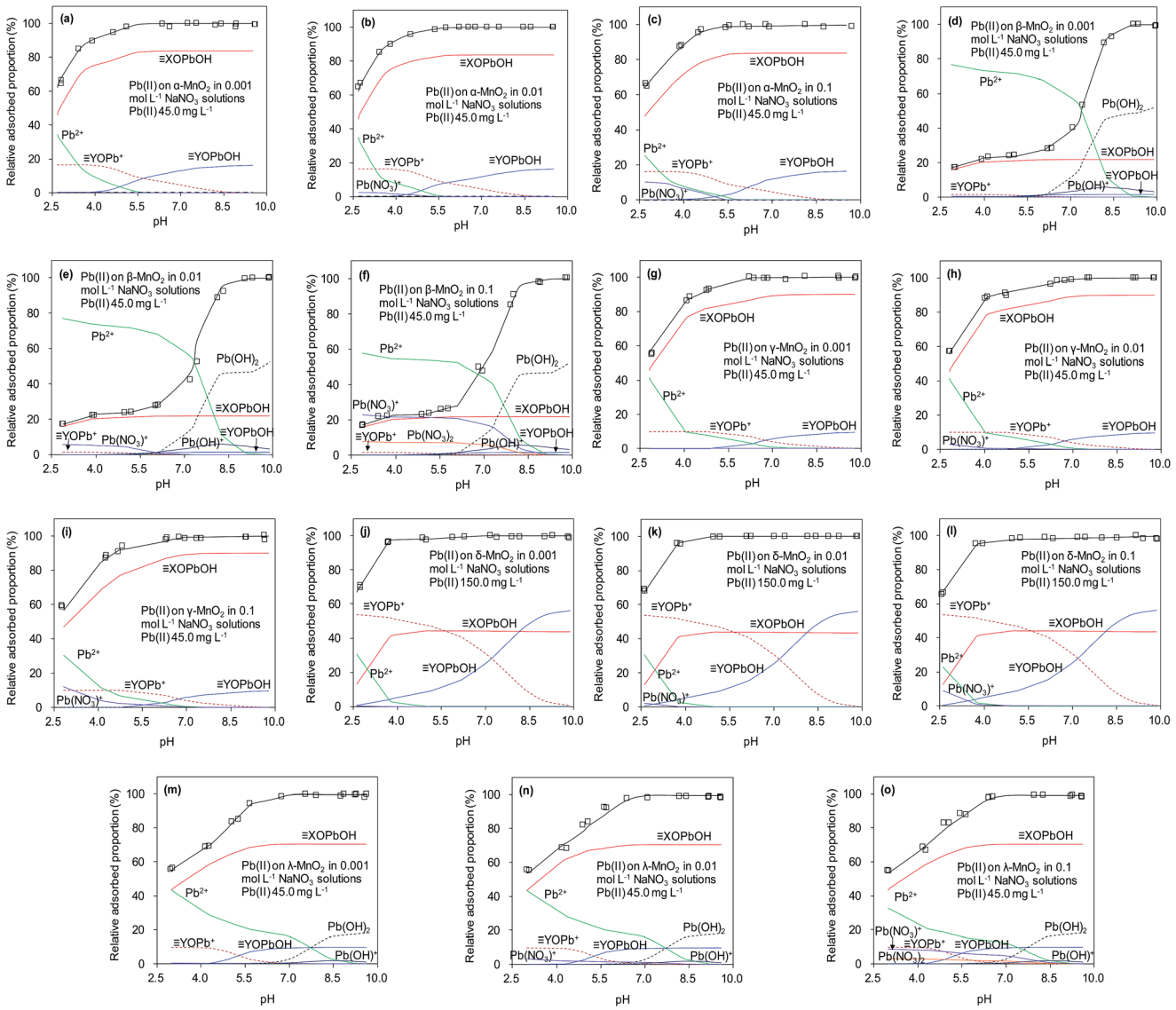

Fig. 9 Surface binding species for Pb(II) adsorbed on the five MnO_2 adsorbents at different solution pH and ionic strengths.

$$Pb^{2+} + 2NO_3^- = Pb(NO_3)_2,\ \log K = 1.4 \quad (10)$$

The equilibrium protonation constants and complexation constants with OH^- and NO_3^- were calculated at the ionic strength of 0.01 mol L^{-1} $NaNO_3$, and these constants were also used for the higher ionic strengths. The predicted aqueous complexation of Pb(II) in 0.001, 0.01 and 0.1 mol L^{-1} $NaNO_3$ solutions was performed using the computer program FITEQL 3.2, and the results are shown in Fig. 9. The amount of $Pb(OH)^+$ species increased with the solution pH, while the amount of $PbNO_3^+$ species increased with ionic strength. According to the literature, the increase of ionic strength facilitated the formation of the $Pb(NO_3)^+$ and $Pb(NO_3)_2$ species,[40] whose amounts increased at higher ionic strength at low pH conditions (<5.0). Moreover, the stability of aqueous Pb(II) complexes was enhanced at high ionic strength, which might suppress the adsorption of Pb(II) on the adsorbents. However, due to the high adsorption capacity of α-, γ-, δ- and λ-MnO_2, the $PbNO_3^+$ and $Pb(OH)^+$ species could also be adsorbed on the negative charged MnO_2 in the tested pH range, suggesting the negligible effect of speciation on Pb(II) adsorption onto α-, γ- and δ-MnO_2. As for β- and λ-MnO_2, the poor Pb(II) adsorption capacity within the pH range of 2.5–5.0 implied that a large amount of $PbNO_3^+$ and $Pb(OH)^+$ complexes remained in the solutions. The residual $PbNO_3^+$ and $Pb(OH)^+$ complexes would precipitate at high pH conditions (>6.0), which was in line with the results of pH effect. Additionally, the observed effect of ionic strength on Pb(II) adsorption on MnO_2 was negligible over the pH range of 2–10, indicating that Pb(II) was adsorbed predominantly *via* inner-sphere complexation. Similar results were also observed by Al Degs *et al.*[42] and Han *et al.*[43] This could be ascribed to the fact that the five MnO_2 adsorbents possessed excellent adsorption selectivity for Pb(II) under the interference of Na(I). Moreover, δ-MnO_2 exhibited a high adsorption capacity of Pb(II) with

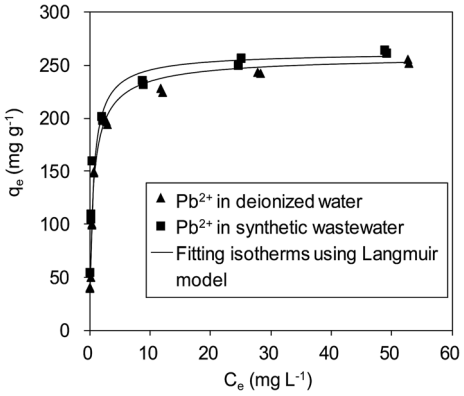

Fig. 10 Adsorption isotherms of Pb(II) on δ-MnO_2 in a synthetic wastewater containing 100 mg L^{-1} of Na(I), 100 mg L^{-1} Mg(II) and 150 mg L^{-1} Ca(II).

outstanding selectivity under high ionic strength, indicating a promising potential for Pb(II) adsorptive removal from wastewaters.

To verify the efficiency of using δ-MnO_2 to remove Pb(II) from real wastewater, Pb(II) adsorption on δ-MnO_2 in a synthetic wastewater containing Na(I) (100.0 mg L^{-1}), Mg(II) (100.0 mg L^{-1}) and Ca(II) (150.0 mg L^{-1}) was studied, and the results are shown in Fig. 10. It is shown that Pb(II) adsorption on the δ-MnO_2 adsorbent slightly increased with the co-existing ions in synthetic wastewater at pH 4.0, further indicating that Pb(II) adsorption was mainly driven by the strong inner-sphere complexation interactions between Pb(II) and the hydroxyl groups on δ-MnO_2.[21] The observed effects of coexisting alkaline/earth metal ions on Pb(II) adsorption to δ-MnO_2 in synthetic wastewater clarified the validity of using δ-MnO_2 as an efficient adsorbent for Pb(II) removal from actual wastewater.

3.5 Modeling the adsorption of Pb(II) onto MnO_2

A number of previous researchers have used the diffuse double layer surface complexation model (SCM) to predict the adsorption of Pb(II) on manganese oxides at different ionic strengths.[44,45] The SCM assumes that only surface complexation occurs on the charged surfaces, consistent with the adsorption mechanism of Pb(II) adsorption to the five MnO_2 adsorbents. Thus, the SCM was chosen to be used in this study to describe the adsorption of Pb(II) to the surface sites on the five MnO_2 adsorbents. The determination of surface equilibrium constants from experimental data was performed using the computer program FITEQL 3.2. The surface hydroxyl groups, including DCS and DES sites, at the five MnO_2 adsorbents surface were determined according to the literature,[44] and the results are listed in Table 4. The content of hydroxyl groups on δ-MnO_2 was observed to be much higher than those of other MnO_2 adsorbents, which resulted from its largest BET surface area. Manganese oxides with a larger BET surface area possessed more site vacancies, resulting in more surface hydroxyl groups. These results suggested that the BET surface area was the predominant factor affecting the content of hydroxyl groups on manganese oxides.

A two-site model is employed to describe the reactions at manganese oxides surface, and the following reactions were used in FITEQL 3.2 to model Pb(II) adsorption on the five MnO_2 adsorbents surface.

On the DCS sites:

$$\equiv XOH + H^+ = \equiv XOH_2^+ \quad (11)$$

$$\equiv XOH = \equiv XO^- + H^+ \quad (12)$$

$$\equiv XOH_2^+ + Pb^{2+} = \equiv XOPb^+ + 2H^+ \quad (13)$$

$$\equiv XO^- + Pb^{2+} + H_2O = \equiv XOPbOH + H^+ \quad (14)$$

On the DES sites:

$$\equiv YOH + H^+ = \equiv YOH_2^+ \quad (15)$$

$$\equiv YOH = \equiv YO^- + H^+ \quad (16)$$

$$\equiv YOH^{2+} + Pb^{2+} = \equiv YOPb^+ + 2H^+ \quad (17)$$

$$\equiv YO^- + Pb^{2+} + H_2O = \equiv YOPbOH + H^+ \quad (18)$$

The FITEQL failed to simulate the surface species on the five MnO_2 adsorbents because the species $\equiv XOH_2^+$ did not exist below the IEP of MnO_2.[42] The zeta potential analysis showed that the IEP values of the five MnO_2 adsorbents were all below tested solution pH, suggesting that the $\equiv XOH_2^+$ and $\equiv XOPb^+$ would not be significant species in the present study. Thus, the reaction $\equiv XOH_2^+ + Pb^{2+} = \equiv XOPb^+ + 2H^+$ was ignored in this study. All the parameters used to simulate the acid–base chemistry of the five MnO_2 adsorbents are summarized in Table 4.

Fig. 9 presents predicted the surface binding species for Pb(II) adsorbed onto the five MnO_2 adsorbents in 0.001, 0.01 and 0.1 mol L^{-1} $NaNO_3$. It is apparent that the fitted curves

Table 4 Parameters for modeling the acid–base surface chemistry of MnO_2 adsorbents

Sorbents	S_{BET} (m^2 g^{-1})	≡XOH (mmol g^{-1})	≡YOH (mmol g^{-1})	log $K_{\equiv XO^-}$	log $K_{\equiv YO^-}$	log $K_{\equiv YOH_2^+}$
α-MnO_2	97.5	0.1996	0.0355	−0.86	−1.45	4.35
β-MnO_2	14.2	0.0477	0.0333	−1.24	−1.91	4.61
γ-MnO_2	71.4	0.1993	0.0214	−1.25	−2.67	4.71
δ-MnO_2	270.8	0.7093	0.4090	−1.76	−4.52	2.57
λ-MnO_2	36.6	0.1528	0.0208	−1.44	−1.28	4.28

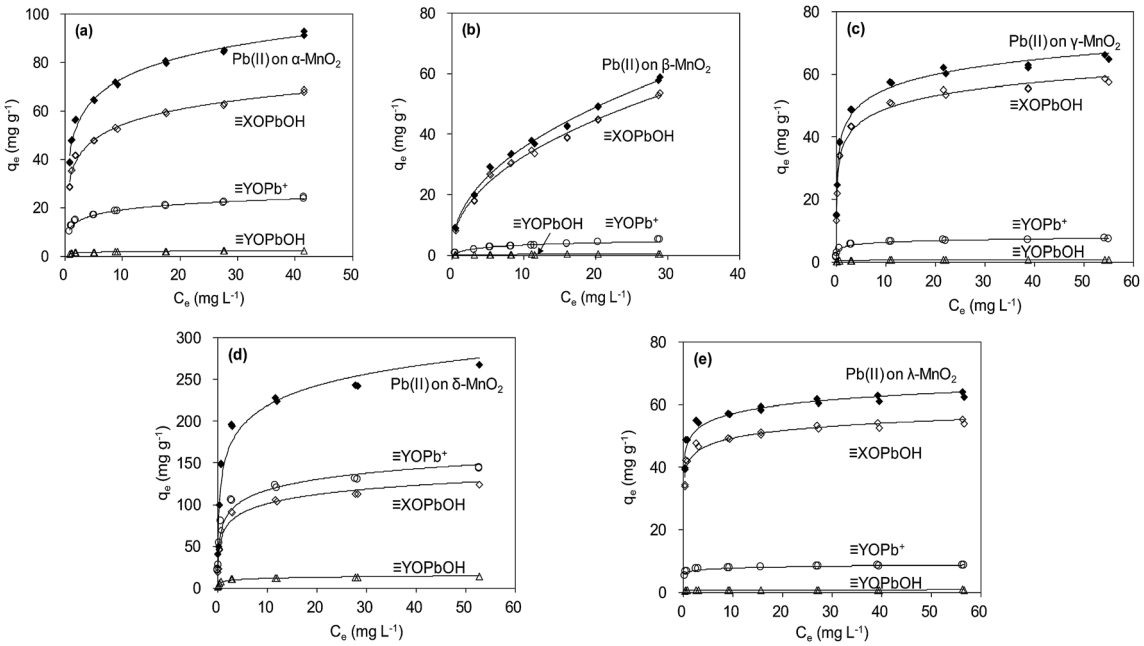

Fig. 11 Modeling Pb(II) adsorption isotherms using diffuse double layer surface complexation model (SCM).

provided a close description of Pb(II) adsorption on the five MnO_2 adsorbents over the tested pH range. Within the pH range of 2.5–10.0, ≡XOPbOH was the predominant species on α-, β-, γ- and λ-MnO_2 surfaces, while ≡YOPb$^+$ made insignificant contributions to adsorption at acidic to neutral pH conditions. The ≡YOPb$^+$ species decreased with the increase of solution pH, probably because the OH^- species increased at higher pH conditions and would bind to the ≡YOPb$^+$, resulting in the increase of ≡YOPbOH species on α-, β-, γ- and λ-MnO_2 surfaces. For δ-MnO_2, ≡YOPb$^+$ was the predominant species over the pH range of 2.5–5.8, likely due to the large amount of ≡YOH groups on the layered structural surfaces. Notably, $Pb(OH)_2$ species appeared on the surface of β- and λ-MnO_2 at high pH conditions, suggesting the Pb(II) had precipitated. This is conceivably attributed to the insufficient hydroxyl groups on β- and λ-MnO_2 surfaces for Pb(II) adsorption.

The adsorption isotherm data were reproduced by using parameters estimated from SCM, and the results are shown in Fig. 11. According to the fitting results from SCM, $Pb(OH)^+$ and $Pb(OH)_2$ precipitate did not present at low pH conditions (<6.0) (Fig. 9). The aqueous Pb(II) species were Pb^{2+} and $Pb(NO_3)^+$. For α-, β-, γ- and λ-MnO_2, ≡XOPbOH was the dominant species contributing to Pb(II) adsorption at the tested Pb(II) concentration in deionized water. This is likely due to the high Pb(II) concentration in the adsorption isotherm experiment. Similar results were also reported by Usiyama and Fukushi.[41] As for δ-MnO_2, prediction of surface speciation showed that the ≡YOPb$^+$ was the dominant species at various Pb(II) concentrations. The difference of dominant surface speciation between δ-MnO_2 and other MnO_2 adsorbents was possibly attributed to the high content of DES adsorption sites and high cation exchange capacity on layered manganese oxides.

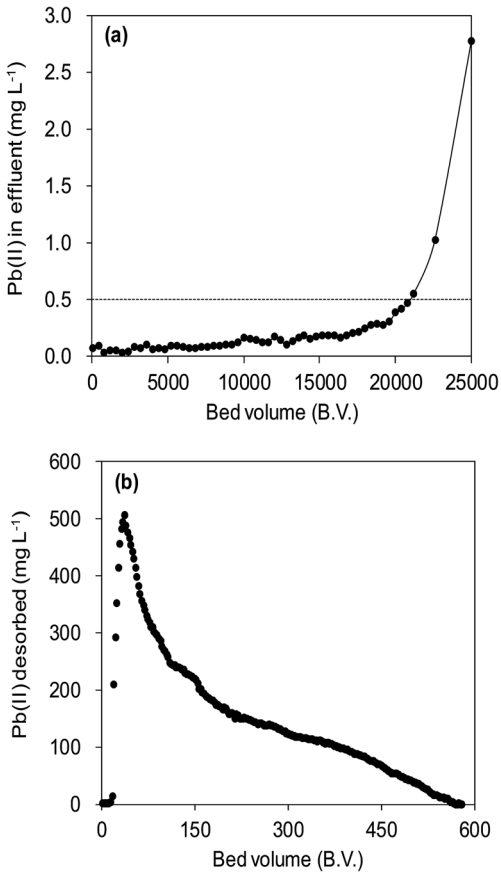

Fig. 12 Fixed-bed column adsorption and regeneration test. (a) Pb(II) removal from a synthetic wastewater by a column bed packed with δ-MnO_2. Influent Pb(II) was 20 mg L^{-1} with 100 mg L^{-1} of Na(I), 100 mg L^{-1} Mg(II), and 150 mg L^{-1} Ca(II), and the flow rate was 15.0 mL h^{-1}. (b) Regeneration of Pb(II) preloaded δ-MnO_2 using a mix solution containing 0.1 mol L^{-1} HNO_3 and 5% (wt) $Ca(NO_3)_2$, and the flow rate was 7.5 mL h^{-1}.

Table 5 Estimated parameters of Thomas and Yoon–Nelson models for the sorption of Pb(II) by the δ-MnO_2 packed column

		Thomas model			Yoon–Nelson model		
C_0 (mg L^{-1})	Flow rate (mL h^{-1})	k_T (L mg^{-1} h^{-1})	Q_m (mg g^{-1})	R^2	k_{YN} (min^{-1})	τ	R^2
20.0	15.0	4.26×10^{-5}	6.27×10^5	0.82	8.52×10^{-4}	7.32×10^3	0.82

3.6 Fixed-bed adsorption

Fig. 12a illustrated an effluent history of δ-MnO_2 fixed-bed column adsorption experiment, which was carried out to evaluate the sorbent applicability in wastewater treatment. The breakthrough point was set as 0.5 mg L^{-1} for Pb(II), as the regulated maximum concentration level by the mining industry emission standard of China.[46] The sorbent exhibited a breakthrough at the point of ~25 000 bed volume (BV) under the experimental conditions, indicated that Pb(II) could be efficiently removed by δ-MnO_2 till the significant breakthrough occurs. The column adsorption behavior of Pb(II) on δ-MnO_2 could be further quantified by the Thomas model and Yoon–Nelson model. The Thomas model can be expressed as follows:[47]

$$\ln\left(\frac{C_0}{C} - 1\right) = \frac{k_T Q_m M}{F} - k_T C_0 t \tag{19}$$

The Yoon–Nelson model is given in eqn (20).[48]

$$\ln \frac{C}{C_0 - C} = k_{YN} t - \tau k_{YN} \tag{20}$$

where C_0 is influent Pb(II) concentration (mg L^{-1}), C is effluent Pb(II) concentration (mg L^{-1}) at time t (h), k_T (L mg^{-1} h^{-1}) and k_{YN} (min^{-1}) are the kinetic constants of Thomas model and Yoon–Nelson model, respectively, Q_m is the maximum solid-phase concentration of the solute (mg g^{-1}), M is the sorbents packed in the column (g), F is the flow rate (mL h^{-1}), and τ is the time required for 50% adsorbate breakthrough (h).

The fitting parameters of experimental data are summarized in Table 5. From the regression coefficients it could be concluded that the Thomas and Yoon–Nelson models fitted the experimental data accurately. As was not observed in the present study, the column breakthrough capacity was estimated using the Thomas model according to the literature.[48] The Pb(II) adsorption capacity at the breakthrough point was 6.27×10^5 mg g^{-1}, which was much higher than the values reported for hydrous Zr(IV) oxide-based nanocomposite (319.4 mg g^{-1}) and polyacrylamide–hydrated ferric oxide hybrid material (211.4 mg g^{-1}).[48,49] Considering the structure of δ-MnO_2, the higher adsorption capacity was likely due to the capillary condensation, which was used advantageously as universal functionalization strategy in nanoparticle thin films assembled layer-by-layer.[49] The value of τ was as large as 7.32×10^3 h, also remarkably larger than the reported values.[50,51] These results indicate that δ-MnO_2 is highly effective for removal of Pb(II) from water in both batch and fixed-bed mode. Notably, the synthetic method of δ-MnO_2 in this study was simple, economic, environmentally friendly, and was suitable for large-scale production. Therefore, δ-MnO_2 could be applied as a cost-effective adsorbent for the adsorptive removal of Pb(II) from wastewater.

The suppressed adsorption of Pb(II) on δ-MnO_2 observed at low pH implied that acidic treatment was a feasible approach to regenerating the Pb(II)-loaded adsorbent. The mixed regenerant of 0.1 mol L^{-1} HNO_3 and 5 wt% wt $Ca(NO_3)_2$ was used for the exhausted δ-MnO_2 column regeneration at room temperature, and the results are showed in Fig. 12b. The cumulative desorption efficiency was around 20%, and about 80% of Pb(II) preloaded by δ-MnO_2 could not be effectively desorbed by the regeneration solution. Such low desorption ratio suggested that the adsorption sites of δ-MnO_2 were irreversible and could not be reused. Li *et al.*[35] and Pan *et al.*[52] investigated the adsorption sites of δ-MnO_2 by EXAFS and found two distinct sites of δ-MnO_2 for heavy metal ions adsorption. They concluded that the edge-linkage inner-sphere complexation were irreversible, while the corner-linkage mode was reversible. Additionally, the ionic strengths effects proved surface complexes were formed by Pb(II) and surface adsorption sites. Thus, we suggested that the edge-linkage inner-sphere complexes were responsible for the irreversible Pb(II) adsorption by δ-MnO_2. Moreover, the ability of δ-MnO_2 fixed-bed column to efficiently remove Pb(II) from synthetic wastewaters makes it a good system for large-scale application.

4. Conclusions

In this work, we investigated the adsorption behavior of Pb(II) on five manganese oxides with different crystallographic phases. δ-MnO_2 showed the highest adsorption capacity due to its high BET surface area and layered structure which was fully accessible for Pb(II). Additionally, the large interlayer spacing and high amount of surface chemisorbed oxygen enhanced the Pb(II) adsorption on δ-MnO_2. On the contrary, adsorption capacities of porous α-, β-, γ- and λ-MnO_2 were constrained by the low efficiency of pores and Pb(II) was mainly adsorbed on the external surfaces. The adsorption kinetics of Pb(II) on MnO_2 adsorbents followed the pseudo-second-order model, and the adsorption of δ-MnO_2 was no affected by coexisting cations in water. The hydroxyl groups on the MnO_2 surface undergo pH dependent inner-sphere surface complexation reactions. The predominant species on α-, β-, γ- and λ-MnO_2 surfaces was ≡XOPbOH, while the ≡YOPb$^+$ species was the predominant species on δ-MnO_2 surface over the pH range of 2.5–5.8. Column test verified the high working adsorption capacity and durability of δ-MnO_2 and therefore highlighted its promising potential as an effective adsorbent for the removal of heavy metal ions in water.

Conflicts of interest

There are no conflicts of interest to declare.

Acknowledgements

Financial support from the Special S&T Project on Treatment and Control of Water Pollution of China (No. 2017ZX07201005) is gratefully acknowledged.

References

1 M. Liu, Y. Wang, L. Chen, Y. Zhang and Z. Lin, *ACS Appl. Mater. Interfaces*, 2015, **7**, 7961–7969.
2 C. H. Yan, J. Xu and X. M. Shen, *Environ. Health Perspect.*, 2013, **121**, A294–A295.
3 S. Hou, L. Yuan, P. Jin, B. Ding, N. Qin, L. Li, X. Liu, Z. Wu, G. Zhao and Y. Deng, *Theor. Biol. Med. Modell.*, 2013, **10**, 13.
4 World Health Organization, *Guidelines for Drinking-water Quality, Incorporating The First and Second Addenda*, 3rd edn, 2008, vol. 1, http://www.who.int/water_sanitation_health/dwq/fulltext.pdf.
5 Z. X. Wu and D. Y. Zhao, *Chem. Commun.*, 2011, **47**, 3332–3338.
6 X. Gu, L. J. Evans and S. J. Barabash, *Geochim. Cosmochim. Acta*, 2010, **74**, 5718–5728.
7 C. C. Wang, L. C. Juang, C. K. Lee, T. C. Hsu, J. F. Lee and H. P. Chao, *J. Colloid Interface Sci.*, 2004, **280**, 27–35.
8 D. Dong, Y. M. Nelson, L. W. Lion, M. L. Shuler and W. C. Ghiorse, *Water Res.*, 2000, **34**, 427–436.
9 L. D. Puppa, M. Komárek, F. Bordas, J. C. Bollinger and E. Joussein, *J. Colloid Interface Sci.*, 2013, **399**, 99–106.
10 Y. Wang, X. Feng, M. Villalobos, W. Tan and F. Liu, *Chem. Geol.*, 2012, **292–293**, 25–34.
11 S. M. Maliyekkal, K. P. Lisha and T. Pradeep, *J. Hazard. Mater.*, 2010, **181**, 986–995.
12 R. M. McKenzie, *Soil Res.*, 1981, **19**, 41–50.
13 J. W. Tonkin, L. S. Balistrieri and J. W. Murray, *Appl. Geochem.*, 2004, **19**, 29–53.
14 Y. C. Son, V. D. Makwana, A. R. Howell and S. L. Suib, *Angew. Chem., Int. Ed.*, 2001, **40**, 4280–4283.
15 M. Yano, S. Suzuki, M. Miyayama and M. Ohgaki, *Solid State Ionics*, 2013, **233**, 32–37.
16 X. B. Luo, K. Zhang, J. M. Luo, S. L. Luo and J. Crittenden, *Environ. Sci. Technol.*, 2016, **50**, 13002–13012.
17 M. G. Kozlova, S. V. Balakhonov, E. A. Goodilin, B. R. Churaulov, A. G. Veresov and Y. D. Tret'yakov, *Russ. Chem. Bull.*, 2008, **57**, 1151–1156.
18 G. V. Korshin, H. S. Chang, A. I. Frenkel and J. F. Ferguson, *Environ. Sci. Technol.*, 2007, **41**, 2560–2565.
19 J. Al Abdullah, A. G. Al Lafi, W. Al Masri, Y. Amin and T. Alnama, *Water, Air, Soil Pollut.*, 2016, **227**, 1–14.
20 X. Wang and Y. D. Li, *Chemistry*, 2003, **9**, 300–306.
21 H. P. Zhang, L. Q. Gu, L. Zhang, S. R. Zheng, H. Q. Wan, J. Y. Sun, D. Q. Zhu and Z. Y. Xu, *Appl. Surf. Sci.*, 2017, **406**, 330–338.
22 H. Chen, Y. Wang and Y. K. Lv, *RSC Adv.*, 2016, **6**, 54032.
23 H. M. Xu, Z. Qu, S. J. Zhao, J. Mei, F. Q. Quan and N. Q. Yan, *J. Hazard. Mater.*, 2015, **299**, 86–93.
24 Q. H. Zhang, S. Sun, S. Li, H. Jiang and J. G. Yu, *Chem. Eng. Sci.*, 2007, **62**, 4869–4874.
25 S. B. Kanungo and K. M. Parida, *J. Colloid Interface Sci.*, 1984, **98**, 245–251.
26 D. M. Robinson, Y. B. Go, M. Greenblatt and G. C. Dismukes, *J. Am. Chem. Soc.*, 2010, **132**, 11467–11469.
27 L. P. Kang, M. M. Zhang, Z. H. Liu and K. Ooi, *Spectrochim. Acta, Part A*, 2007, **67**, 864–869.
28 W. A. Jefferson, C. Hu, H. Liu and J. Qu, *Chemosphere*, 2015, **119**, 1–7.
29 H. W. Nesbitt, G. W. Canning and G. M. Bancroft, *Geochim. Cosmochim. Acta*, 1998, **62**, 2097–2110.
30 S. M. Ponder, J. C. Darab and T. E. Mallouk, *Environ. Sci. Technol.*, 2000, **34**, 2564–2569.
31 Z. Rao, K. Feng, B. Tang and P. Wu, *ACS Appl. Mater. Interfaces*, 2017, **9**, 2594–2605.
32 D. C. Golden, C. C. Chen and J. B. Dixon, *Clays Clay Miner.*, 1987, **35**, 271–278.
33 H. S. Kim and P. C. Stair, *J. Phys. Chem. B*, 2004, **108**, 17019–17026.
34 K. D. Kwon, K. Refson and G. Sposito, *Geochim. Cosmochim. Acta*, 2010, **74**, 6731–6740.
35 X. Li, G. Pan, Y. Qin, T. Hu, Z. Wu and Y. Xie, *J. Colloid Interface Sci.*, 2004, **271**, 35–40.
36 A. Perner, K. Holl, D. Ilic and M. Wohlfahrt-Mechrens, *Eur. J. Inorg. Chem.*, 2002, **5**, 1108–1114.
37 M. Sekar, V. Sakthi and S. Rengaraj, *J. Colloid Interface Sci.*, 2004, **279**, 307–313.
38 J. Wang, S. Zheng, Y. Shao, J. Liu, Z. Xu and D. Zhu, *J. Colloid Interface Sci.*, 2010, **349**, 293–299.
39 M. B. Jazi, M. Arshadi, M. J. Amiri and A. Gil, *J. Colloid Interface Sci.*, 2014, **422**, 16–24.
40 T. Usiyama and K. Fukushi, *Geochim. Cosmochim. Acta*, 2016, **190**, 134–155.
41 A. M. Puziy, O. I. Poddubnaya, V. N. Zaitsev and O. P. Konoplitska, *Appl. Surf. Sci.*, 2004, **221**, 421–429.
42 Y. Al Degs, M. A. M. Khraisheh and M. F. Tutunji, *Water Res.*, 2001, **35**, 3724–3728.
43 R. Han, W. Zou, Z. Zhang, J. Shi and J. Yang, *J. Hazard. Mater.*, 2006, **137**, 384–395.
44 P. J. Pretorius and P. W. Linder, *Appl. Geochem.*, 2001, **16**, 1067–1082.
45 J. W. Tonkin, L. S. Balistrieri and J. W. Murray, *Appl. Geochem.*, 2004, **19**, 29–53.
46 *Integrated Water Discharge Standard*, Ministry of the People's Republic of China, Beijing, 1996.
47 H. C. Thomas, *J. Am. Chem. Soc.*, 1944, **66**, 1664–1666.
48 J. F. Costa, V. J. Vilar, C. M. Botelho, E. A. Da Silva and R. A. Boaventura, *Water Res.*, 2010, **44**, 3946–3958.
49 M. Hua, Y. N. Jiang, B. Wu, B. C. Pan, X. Zhao and Q. X. Zhang, *ACS Appl. Mater. Interfaces*, 2013, **5**, 12135–12142.
50 F. Fu and Q. Wang, *J. Environ. Manage.*, 2011, **92**, 407–418.
51 H. L. Lu, W. H. Zhang, Y. X. Yang, X. F. Huang, S. Z. Wang and R. L. Qiu, *Water Res.*, 2012, **46**, 854–862.
52 G. Pan, Y. Qin, X. Li, T. Hu, Z. Wu and Y. Xie, *J. Colloid Interface Sci.*, 2004, **271**, 28–34.

